SUPPLEMENTARY INFORMATION

Informing Rational Design of Graphene Oxide through Surface Chemistry Manipulations: Properties Governing Electrochemical and Biological Activities

Yan Wang[1], Leanne M. Gilbertson[1*]

[1]*Department of Civil and Environmental Engineering, University of Pittsburgh, Pittsburgh, PA 15261*

Revised for Submission to:

Green Chemistry
Themed Issue: 2017 Emerging Investigators

March 21, 2017

Pages S1-S22

Table S1

Figures S1-S13

*Corresponding Author: Phone: (412) 624-1683, e-mail: leanne.gilbertson@pitt.edu

1. INTRODUCTION

While high cytotoxicity of GO/rGO materials has been reported in several studies[1-4], their biocompatibility and utility as a growth substrate has also been demonstrated.[5] These discrepancies may be attributed to, i) the different synthesis methods of GO/rGO materials, which can result in different structure and physicochemical properties (e.g., sheet dimensions, surface chemistry, charge transfer capability)[4, 6], and/or ii) the use of different model organism or measured endpoints. Yet, inconsistencies remain when comparing results from studies using the same organism and measured endpoint as demonstrated by the range in relative trends in GO and rGO studies using the acellular GSH oxidation assay (compiled and compared in Table S1).[1, 2, 7]

Table S1. Compiled results from studies of GO/rGO-mediated glutathione (GSH) oxidation using the same method reported in the current study (i.e., Ellman's assay).

Reference number	GO/rGO concentration (mg mL^{-1})	GSH concentration (mM)	Exposure time (hr)	GSH oxidation		
				GO	rGO	Comparison
[2]	0.05	0.4	3	49-71%		
[1]	0.04	0.4	2	22.2%	94.2%	GO < rGO
[7]	0.50	0.4	2	~83%	~73%	GO > rGO

2. EXPERIMENTAL

2.1 Preparation of GO/rGO samples

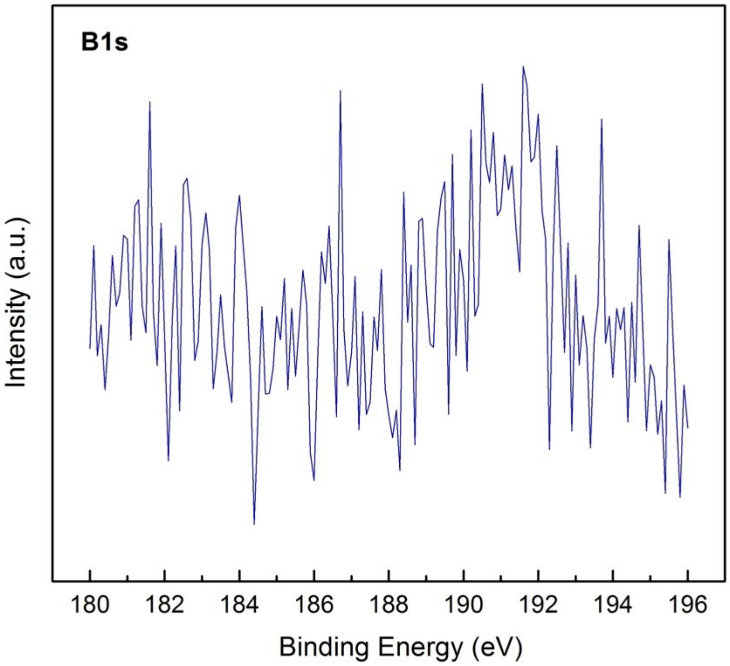

Figure S1. High resolution XPS spectrum of the boron region (B1s) for CGO. No peak signal was detected, indicating the absence of boron in the CGO sample.

2.2 Characterization of GO/rGO samples

Atomic Force Microscopy (AFM). AFM images were taken in tapping mode with an Asylum MFP-3D AFM equipped with a MikroMasch NSC14 silicon cantilever (5.7 N/m force constant and a resonance frequency of 160 kHz). The sample for AFM was prepared by drop-casting 3 µL of a GO/rGO suspension (25 µg mL^{-1}) on a 1.5 cm × 1.5 cm silicon wafer previously cleaned by acetone, methanol, isopropanol, and plasma oxygen. The Asylum research MFP-3D software was used to determine the sheet height and lateral size distribution by counting approximately 100-150 sheets captured in multiple similar images.

Thermogravimetric Analysis (TGA). Thermal stability and purity of ARGO was evaluated by a SDT-Q600 thermal analyzer (TA Instruments, New Castle, DE, USA) under nitrogen and air atmospheres, respectively. Samples were held at 100 °C for 30 min to remove the adsorbed water molecules. The temperature was then increased to 1000 °C at a heating rate of 5 °C min^{-1}.

X-ray Photoelectron Spectroscopy (XPS). Surface chemistry and elemental composition of all samples were evaluated by XPS. Approximately 3 mg of GO/rGO sample was dusted onto the sample holder covered with double-sided copper tape and then loaded into a Thermo Scientific ESCALAB 250Xi instrument with monochromatic Al Kα X-ray source (1486.7 eV, spot size 650 µm). A flood gun was used to compensate the surface charge in the case of measuring the insulating or weakly conductive samples, whereby the charges accumulating at the surface from the emission of electrons are neutralized by replenishing electrons from this external flood gun. Survey spectra were collected using a pass energy of 150 eV with a step size of 1.0 eV, and high-resolution spectra for C1s and O1s were collected using a pass energy of 50 eV with a step size of 0.1 eV. At least three measurements in different locations of each sample were carried out. Thermo Scientific Avantage software was used for peak fitting and to calculate the atomic percentage. Spectra were subtracted with a Smart background, which is a Shirley-derived background with the constraint that any point of the actual data should be of a higher intensity than the background. After background subtraction, a mixed Gaussian-Lorentzian product function was used to deconvolute the peaks. In the process of performing the deconvolution to high-resolution C1s spectra, each spectrum was calibrated with respect to the sp^2 component at 284.8 eV. Peak positions were constrained to shift within ±0.2 eV from the assigned binding energy and values of full width at half maximum (FWHM) for all major components were fixed at the same level with ±0.2 eV deviation.

Attenuated Total Reflectance-Fourier Transform Infrared Spectroscopy (ATR-FTIR). Changes in surface chemistry as a function of treatment was further evaluated/confirmed by ATR-FTIR. The spectra were recorded by a FTIR spectrometer (Bruker VERTEX-70LS) and the attached ATR accessory was equipped with ZnSe crystal, the spectral region was scanned from 600 - 4000 cm^{-1} 150 times with 4 cm^{-1} resolution.

Raman Spectroscopy. Raman spectra were acquired on a Horiba Scientific XplorA Raman-AFM/TERS system using a 638-nm laser for excitation. At least three measurements were performed at different locations of each sample. The intensities, FWHMs, and positions of D and G peaks were determined by performing a polynomial baseline subtraction, and then fitting D peak with a Lorentzian character and G peak with a Breit-Wigner-Fano (BWF) function owing to its asymmetry shape.[8, 9]

Electrical Conductivity Measurement. Thin films of GO/rGO samples were prepared for electrical conductivity measurements. 50 mL GO/rGO suspension (0.3 mg mL^{-1}) was vacuum filtered using a mixed cellulose eater membrane (Millipore) and then dried in a vacuum desiccator with phosphorous pentoxide for 24 hours. The sheet resistance of fabricated films was measured using a four-point probe system (Jandel, Model RM2) connected to a Keithley multimeter for a more accurate display. The film thickness was measured using scanning electron microscopy (SEM, Zeiss Sigma 500 VP). The prepared films were treated with liquid nitrogen to prevent disruption during cutting of the sample (at the measurement sites) to obtain a cross section for thickness determination. The electrical conductivity of samples was obtained from the inverse of the resistivity as determined by both the sheet resistance and the film thickness.

2.3 GO/rGO-mediated GSH Oxidation

GO/rGO dispersions, 0.025 or 0.050 mg mL^{-1} (two concentrations were studied to evaluate mass-dependence), were prepared by bath sonication (VWR Aquasonic 150T) for 30 min in 33 mM bicarbonate buffer (pH=8.6), after which GSH stock solution was added to the prepared triplicate samples to yield a final concentration of 0.4 mM. Next, the sample vials were covered with aluminum foil to avoid potential photo-induced oxidation, and placed on a rotator for continuous rotation for the duration of the experiment. An aliquot was removed at specific time points and filtered (0.22 μm syringe filter) to prevent potential confounding interaction with Ellman's reagent and potential interference with absorbance measurements. Ellman's reagent (5,5'-dithio-bis-(2-nitrobenzoic acid)) was added, which reacts with thiol group of GSH, to produce a yellow product. The absorbance (412 nm) was measured and then used to determine the concentration of GSH remaining in solution. The percent loss of GSH was calculated by comparing with the negative control (no GO/rGO).

The dispersed aggregate size and size distribution was determined by dynamic light scattering (DLS) using a Litesizer 500 (Anton Paar, Austria). Zeta potential was determined using the same instrument and determined by electrophoretic light scattering (ELS). The GO/rGO materials were prepared in the experimental media used for the GSH experiment (no addition of GSH) and transferred to disposable cuvettes for particle size measurements, and to omega cuvettes for zeta potential measurements. The size distribution was determined using a multiexponential fit of the correlation function with a Tikhonov regularized non-negativity constraint, which generates a size distribution without any assumption of the shape (e.g., normal distribution is not assumed). Furthermore, this advanced cumulant method can generate multimodal size distributions and thus, is particularly useful for heterogenous samples where more than one main particle (or aggregate) size is present. Smoluchowsiki approximation was adopted to calculate the zeta potential from electrophoretic mobility based on Henry equation, which is commonly used for lamellar-type materials like GO.[10, 11]

2.4 Electrochemical Measurements

A three-electrode cell was used in all measurements with a platinum counter electrode, an Ag/AgCl reference electrode, and a sample modified rotating ring-disk electrode (RRDE) glassy carbon working electrode. The working electrodes were prepared as follows: i) GO/rGO inks were prepared by mixing 2 mg of GO/rGO, 792 μL isopropanol, 8 μL of Nafion (5 wt%) and 1.2 mL deionized water followed by one hour tip/probe sonication (Branson S-450 digital ultrasonic homogenizer) to form a well-dispersed suspension, ii) 10 μL of the dispersed mixture was carefully drop cast onto the glassy carbon disk electrode surface (0.1963 cm^2) and left to dry (approximately 2 hours).

1 M KOH electrolyte solution was used for all oxygen reduction reaction (ORR) experiments. Prior to each measurement, the electrolyte was bubbled with nitrogen for at least 30 min and the working electrode was cleaned by cyclic voltammetry (CV) for 25 cycles sweeping from 0.2 to -1 V. Next, the electrolyte was saturated with oxygen for 30 min before performing RRDE voltammetry.

RRDE voltammetry was conducted from 0.2 to -1 V at a scan rate of 5 mV s^{-1} with varying rotating speeds of 400, 625, 900, 1600, and 2500 rpm. The ring potential was held at 0.5 V. By collecting the polarization curves at each rotating speed, the kinetic limiting current density (J_K, mA cm^{-2}) during ORR was determined based on the Koutecky-Levich (K-L) equation:[12-15]

$$\frac{1}{J} = \frac{1}{J_L} + \frac{1}{J_K} = \frac{1}{B\omega^{1/2}} + \frac{1}{J_K} \tag{1}$$

where,

$$B = 0.62nFC_0(D_0)^{2/3}\nu^{-1/6} \tag{2}$$

$$J_K = nFkC_0 \tag{3}$$

J is the measured current density (mA cm^{-2}), J_L is the diffusion limited current density (mA cm^{-2}), B is the Levich constant, ω is the rotating speed (rad s^{-1}), n is the electron transfer number during ORR, F is the Faraday constant (96,485 Coulomb mol^{-1}), C_0 is the bulk concentration of dissolved oxygen in 1 M KOH solution (0.84×10^{-6} mol cm^{-3}),[16, 17] D_0 is the diffusion coefficient of dissolved oxygen in 1 M KOH solution (1.65×10^{-5} cm^2 s^{-1}),[16, 17] ν is the kinetic viscosity of the electrolyte (0.01 cm^2 s^{-1}). By plotting J^{-1} versus $\omega^{-1/2}$ at different electrode potentials, the J_K can be obtained by extrapolating K-L lines to yield intercepts.

The electron transfer number (n), determined using RRDE technique is more accurate than that using the K-L plots. While the K-L method requires the reaction to be one-step and n to be constant at certain potentials from theoretical viewpoint, RRDE is able to directly measure the amount of H_2O_2 during ORR process and not required to fulfill the assumptions of the K-L method.[14, 18] Therefore, n and the percentage of H_2O_2 released during ORR were determined using the following equations:[12-15]

$$n = \frac{4I_D}{I_D + \frac{I_R}{N}} \tag{4}$$

and

$$\%H_2O_2 = 200 \times \frac{\frac{I_R}{N}}{I_D + \frac{I_R}{N}} \tag{5}$$

where I_D is the measured disk current (mA), I_R is the measured ring current (mA), and N is the H_2O_2 collection coefficient at the ring (25.6%, provided by PINE Research Instrument).

Electroactive surface area of the prepared GO/rGO working electrodes was determined by CV using 10 mM $Fe(CN)_6^{3-/4-}$ in 1 M KCl under N_2 flow, and then estimated using the following Randles-Sevcik equation modified for quasi-reversible redox process,[19-21]

$$I_P = 2.99 \times 10^5 n(\alpha n_a)^{1/2} A C D^{1/2} \upsilon^{1/2} \tag{6}$$

where A is the electroactive surface area (cm^2), I_P is the peak current (A), n is the electron transfer number during the redox reaction (n=1 for the $Fe(CN)_6^{3-/4-}$ redox process), α is the transfer coefficient and assumed to be 0.5,[21] n_a is the number of electrons involved in the charge transfer step (n_a=1), C is the bulk concentration of the reactant (mol cm^{-3}), D is the diffusion coefficient of the reactant (cm^2 s^{-1}), and υ is the scan rate (V s^{-1}). CV measurements were carried out from 0.6 to -0.1 V with various scan rates from 50 to 270 mV s^{-1}. By plotting I_P versus $\upsilon^{1/2}$, A can be calculated from the slope of the line.

3. RESULTS AND DISUCSSION

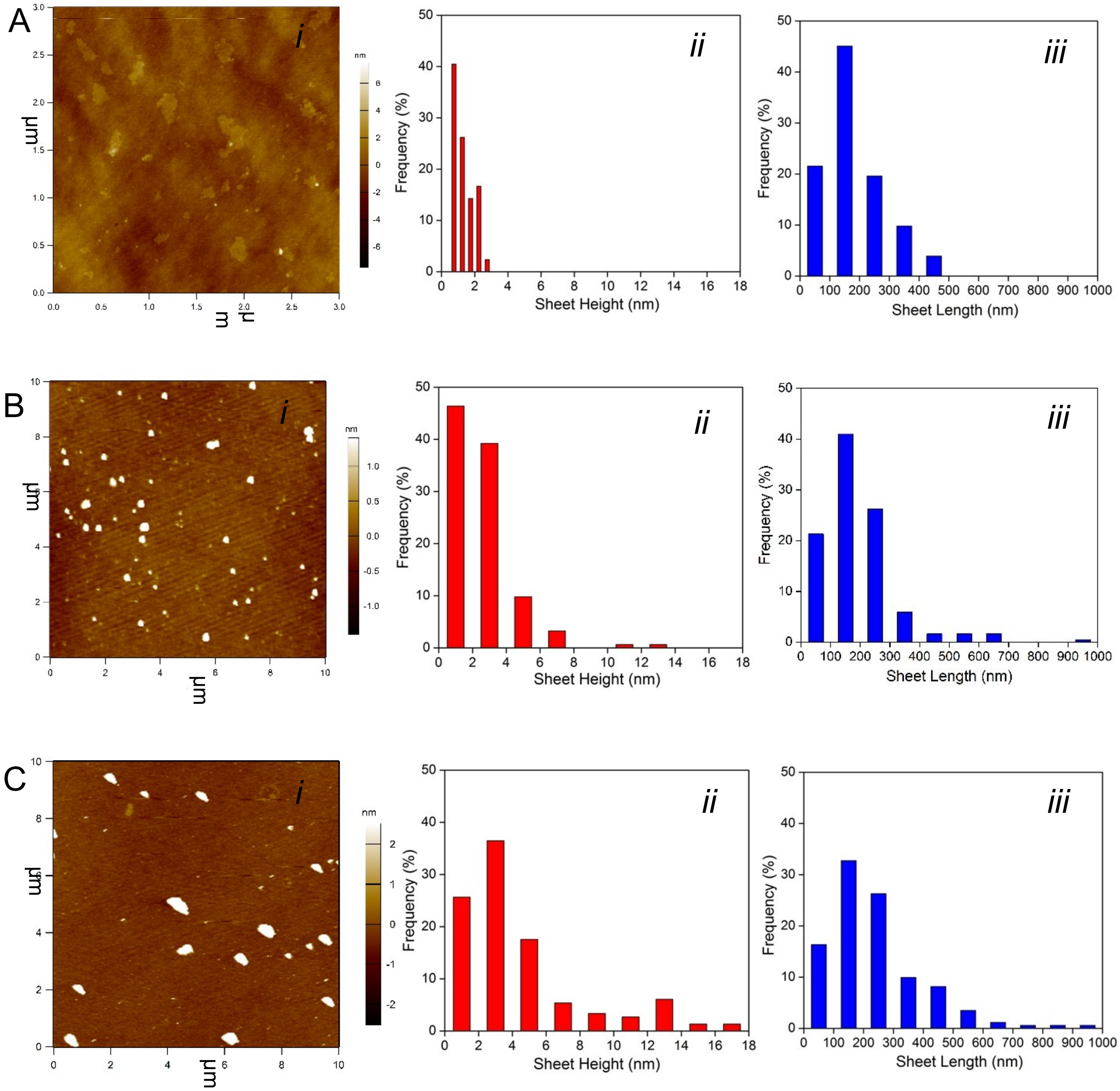

Figure S2. AFM characterization of (A) ARGO, (B) TGO600, and (C) CGO, including representative AFM images (i), sheet height distribution (ii), and lateral size distribution (iii). The histograms were obtained by counting approximately 100-150 sheets captured in multiple images of each sample.

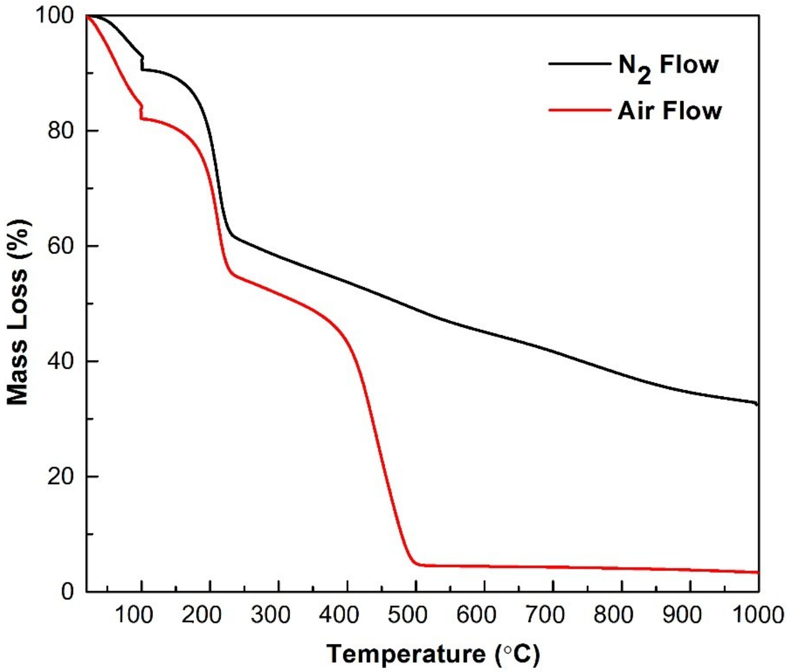

Figure S3. TGA curves of ARGO under nitrogen (black) and air (red) atmosphere.

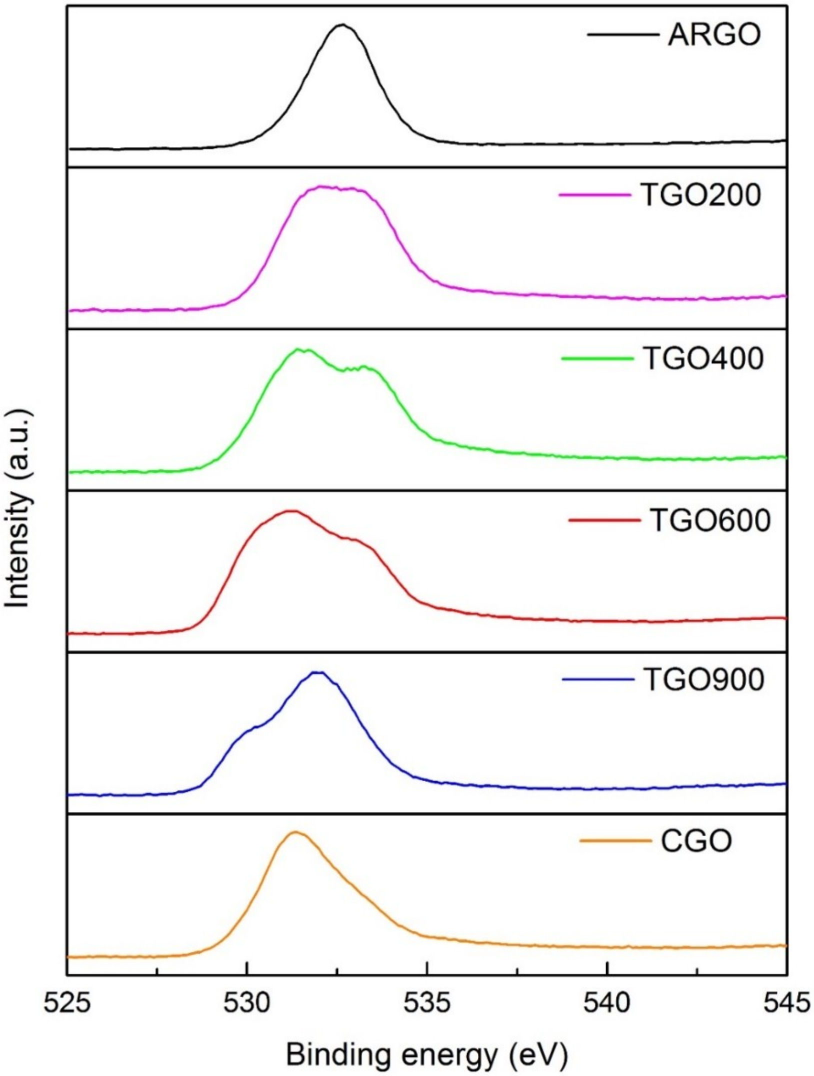

Figure S4. High-resolution O1s spectra of ARGO, TGOs, and CGO.

ATR-FTIR provides complementary insight into surface chemistry and confirms the trends observed by XPS.[22] Compiled spectra are shown in Figure S5. The observed peaks are assigned to characteristic functionalities, as will be described, and consistent with previous reports.[22-26] A broad peak in the 3000 to 3700 cm^{-1} region denotes the -OH stretching mode, which is attributed to bound water molecules, hydroxyl and carboxylic acid groups. Upon reduction, this band is significantly reduced as seen for rGO samples in this region. The two peaks in the region from 1550 to 1730 cm^{-1} correspond to the carbonyl (C=O) stretching mode that arises from the ketone and carboxylic acid groups. While it is challenging to differentiate the contributions of each, the relative intensity of this peak upon reduction confirms the corresponding XPS trends. Significant reduction in the C=O intensity is observed for the TGO600 and TGO900 samples. Peaks within the 980-1150 cm^{-1} region generally represent epoxy (C-O-C) and alkoxy (C-O) bands. C-O moieties decrease remarkably under higher temperature reduction, and evolve as the prominent peak for TGO900, suggesting there are still some carbon-oxygen groups remained even after 900 °C thermal reduction. Indeed, characteristic features localizing in this low-wavenumber region may originate from a number of species including epoxides, ethers, hydroxyls, carboxyls and ketones due to overlapped frequencies.[22] Collectively, it is evident to note the sequent removal of functional groups from the ATR spectra, confirming the XPS results.

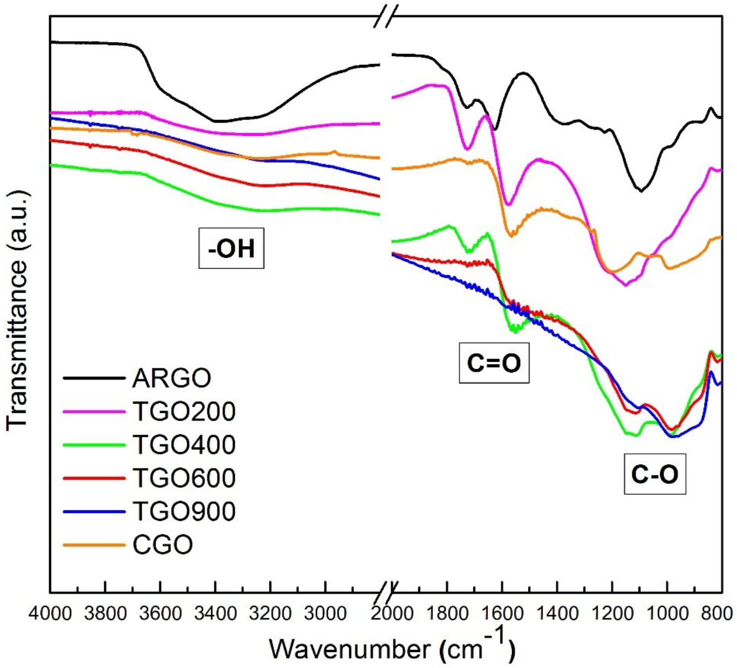

Figure S5. ATR-FTIR spectra of ARGO, TGOs, and CGO.

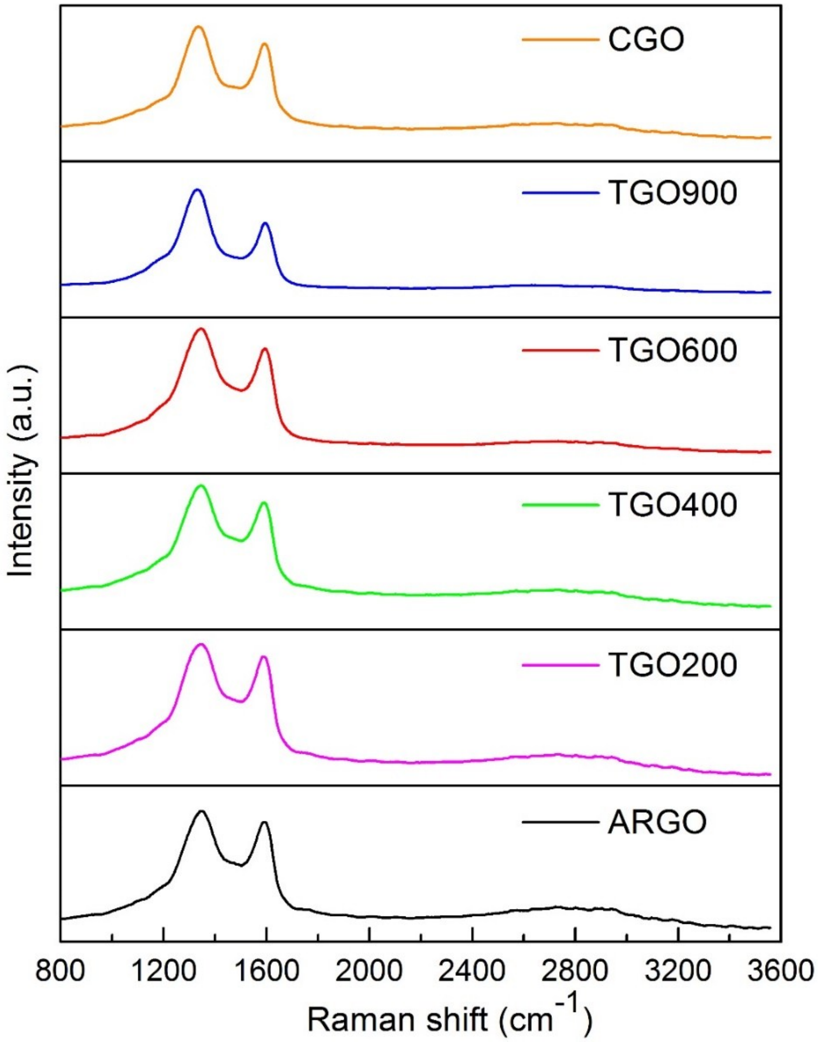

Figure S6. Raman spectra of ARGO, TGOs, and CGO.

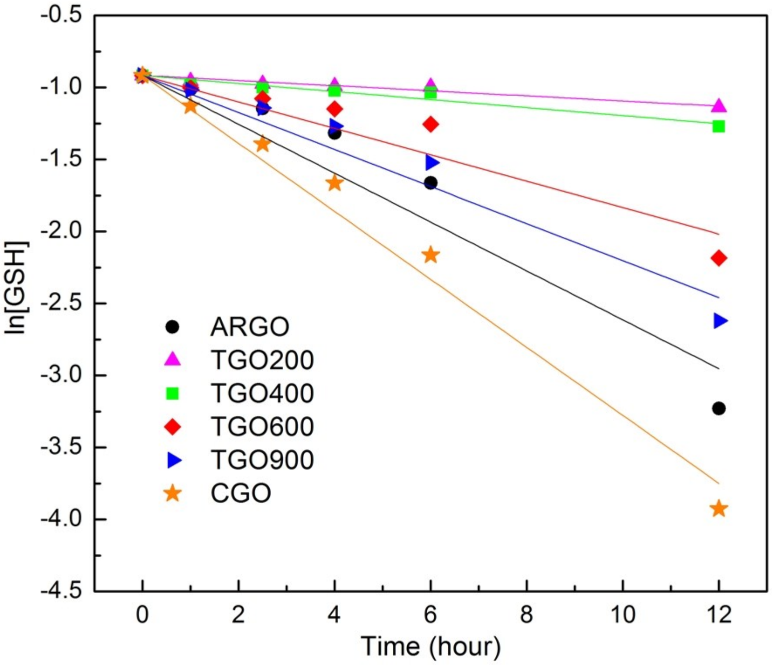

ARGO: $y = -0.1697x - 0.9163,\ R^2 = 0.9820$

TGO200: $y = -0.0177x - 0.9163,\ R^2 = 0.9997$

TGO400: $y = -0.0279x - 0.9163,\ R^2 = 0.9994$

TGO600: $y = -0.0918x - 0.9163,\ R^2 = 0.9892$

TGO900: $y = -0.1286x - 0.9163,\ R^2 = 0.9923$

CGO: $y = -0.2361x - 0.9163,\ R^2 = 0.9950$

Figure S7. Plots of ln[GSH] versus time by applying the first-order kinetic model to the GSH oxidation results for ARGO, TGOs, and CGO. The slope of each fitted line was used to determine the rate constant (*k*).

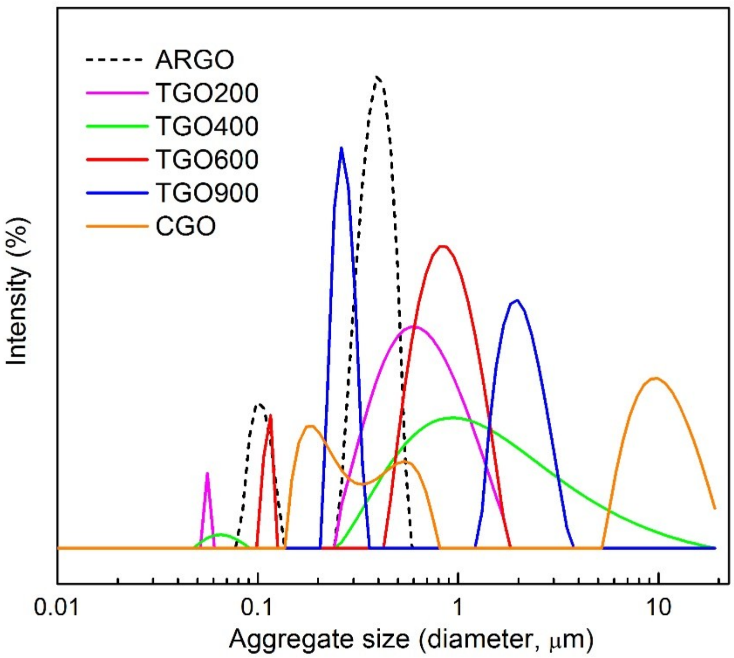

Figure S8. Aggregate size distribution of ARGO, TGOs and CGO as determined by DLS in the GSH-assay scenario. Note that TGOs and CGO might precipitate and settle down to the bottom of cuvettes during the measurement period (~5 min), the contribution to the intensity of the scattered light might not come from all the particles being measured. Consequently, the DLS results for these materials may be underestimated.

Surface charge is likely to change as a function of surface chemistry and thus, is considered as a possible variable in the associated activity. A negative zeta potential is standard for GO and is attributed to the dissociation of electronegative functional groups.[11, 27] In our current study, the pH is adjusted to 8.6 using bicarbonate buffer. As such, the deprotonation of the carboxylic acid group ($pK_a < 4.2$) is primarily responsible for the negative surface charge compared to the more basic groups, such as phenolic groups ($pK_a \sim 10$).[27] No obvious differences in the surface charge were observed among all GO/rGO samples.

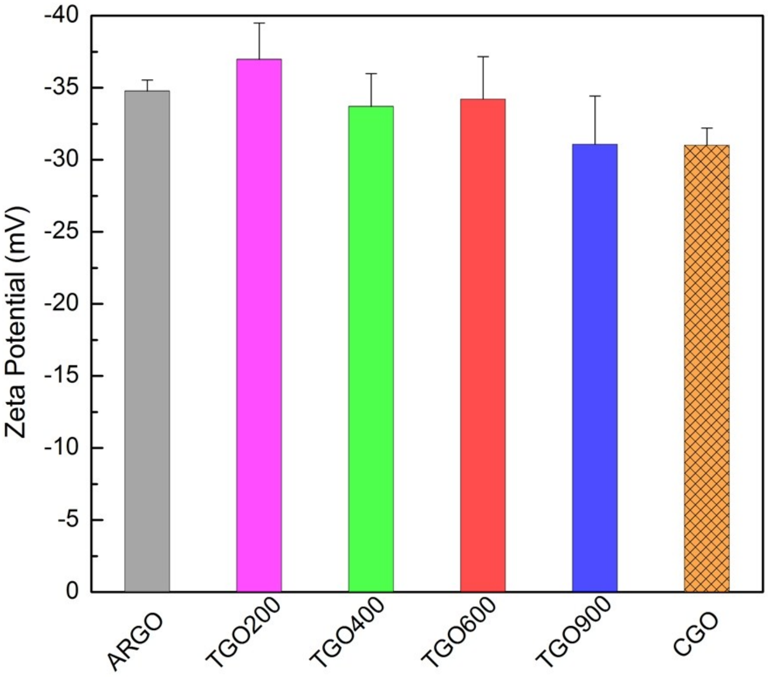

Figure S9. Zeta potentials of ARGO, TGOs and CGO measured by ELS in the GSH-assay scenario.

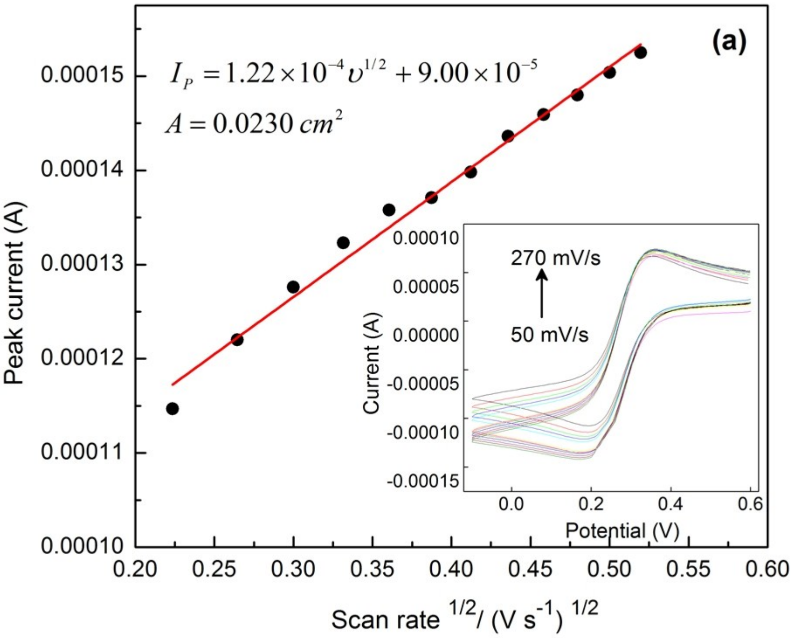
(a)
$I_P = 1.22 \times 10^{-4} \upsilon^{1/2} + 9.00 \times 10^{-5}$
$A = 0.0230\ cm^2$
Peak current (A)
0.00010
0.00011
0.00012
0.00013
0.00014
0.00015
0.20
0.25
0.30
0.35
0.40
0.45
0.50
0.55
0.60
Scan rate $^{1/2}$/ (V s^{-1}) $^{1/2}$
270 mV/s
50 mV/s
Current (A)
0.00010
0.00005
0.00000
-0.00005
-0.00010
-0.00015
0.0
0.2
0.4
0.6
Potential (V)

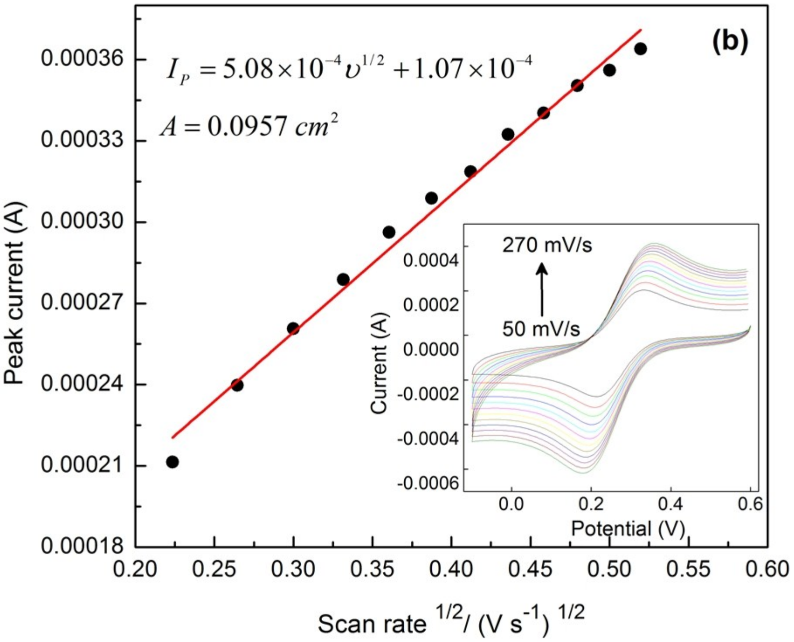
(b)
$I_P = 5.08 \times 10^{-4} \upsilon^{1/2} + 1.07 \times 10^{-4}$
$A = 0.0957\ cm^2$
Peak current (A)
0.00018
0.00021
0.00024
0.00027
0.00030
0.00033
0.00036
0.20
0.25
0.30
0.35
0.40
0.45
0.50
0.55
0.60
Scan rate $^{1/2}$/ (V s^{-1}) $^{1/2}$
270 mV/s
50 mV/s
Current (A)
0.0004
0.0002
0.0000
-0.0002
-0.0004
-0.0006
0.0
0.2
0.4
0.6
Potential (V)

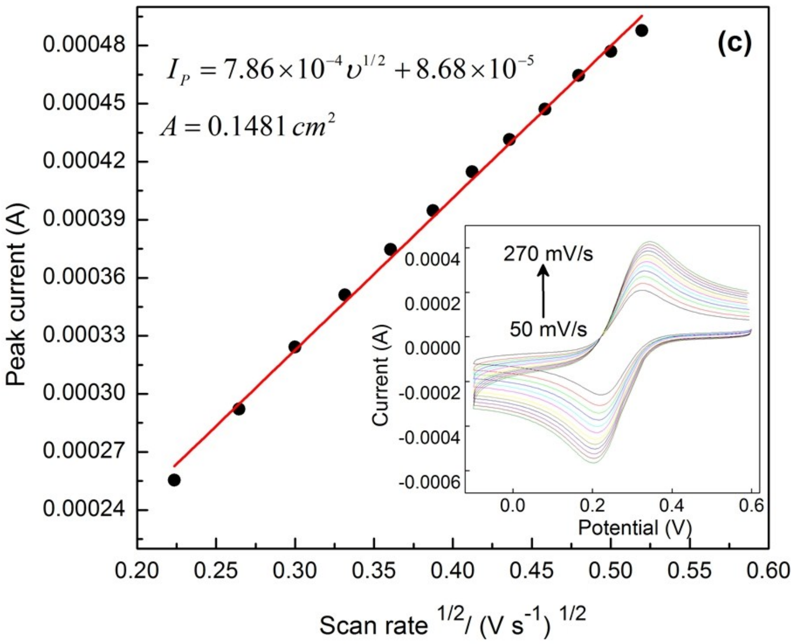
(c)
$I_P = 7.86\times10^{-4}\upsilon^{1/2} + 8.68\times10^{-5}$
$A = 0.1481\,cm^2$
Peak current (A)
0.00024
0.00027
0.00030
0.00033
0.00036
0.00039
0.00042
0.00045
0.00048
0.20
0.25
0.30
0.35
0.40
0.45
0.50
0.55
0.60
Scan rate $^{1/2}$/ (V s^{-1}) $^{1/2}$
270 mV/s
50 mV/s
Current (A)
0.0004
0.0002
0.0000
-0.0002
-0.0004
-0.0006
0.0
0.2
0.4
0.6
Potential (V)

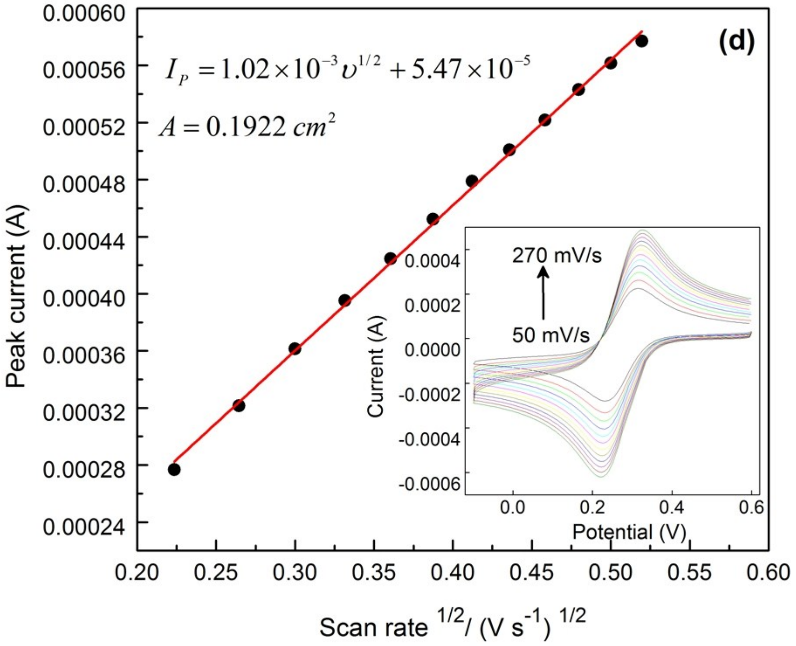
(d)
$I_P = 1.02\times10^{-3}\upsilon^{1/2} + 5.47\times10^{-5}$
$A = 0.1922\,cm^2$
Peak current (A)
0.00024
0.00028
0.00032
0.00036
0.00040
0.00044
0.00048
0.00052
0.00056
0.00060
0.20
0.25
0.30
0.35
0.40
0.45
0.50
0.55
0.60
Scan rate $^{1/2}$/ (V s^{-1}) $^{1/2}$
270 mV/s
50 mV/s
Current (A)
0.0004
0.0002
0.0000
-0.0002
-0.0004
-0.0006
0.0
0.2
0.4
0.6
Potential (V)

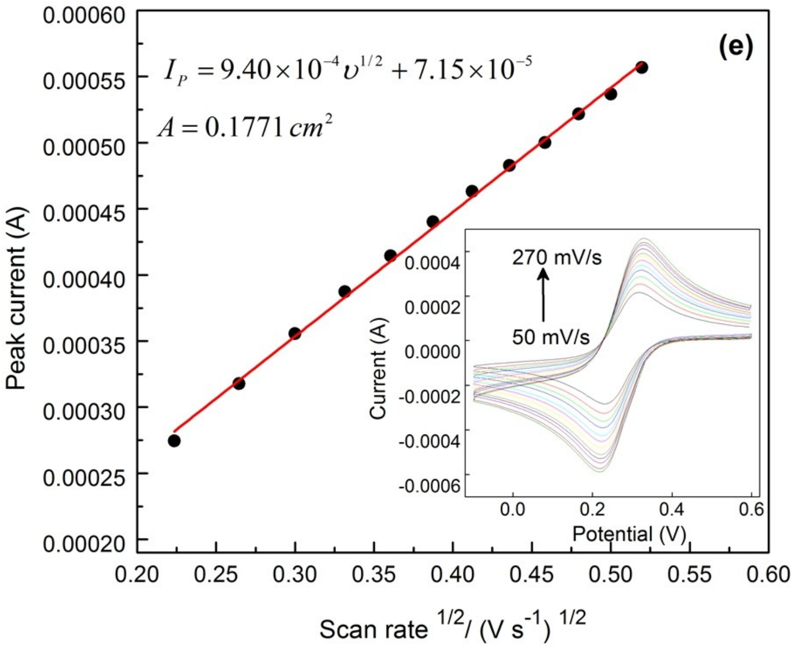

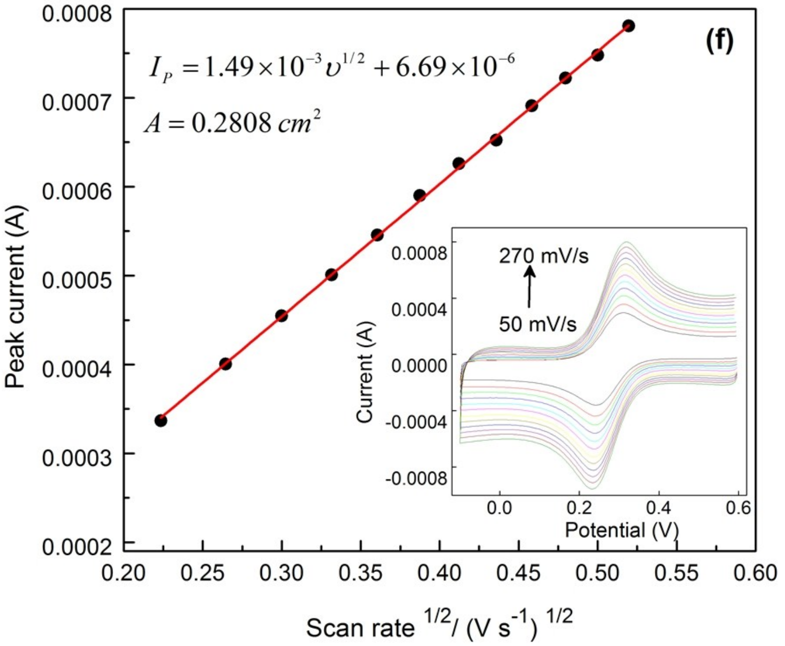

Figure S10. Plots of peak current (I_P) versus (scan rate, ʋ)$^{1/2}$ to estimate electroactive surface areas (*A*) of (a) ARGO, (b) TGO200, (c) TGO400, (d) TGO600, (e) TGO900, and (f) CGO in 10 mM $Fe(CN)_6^{3-/4-}$ /1 M KCl. Insets: CVs at various scan rates from 50 to 270 mV s^{-1}.

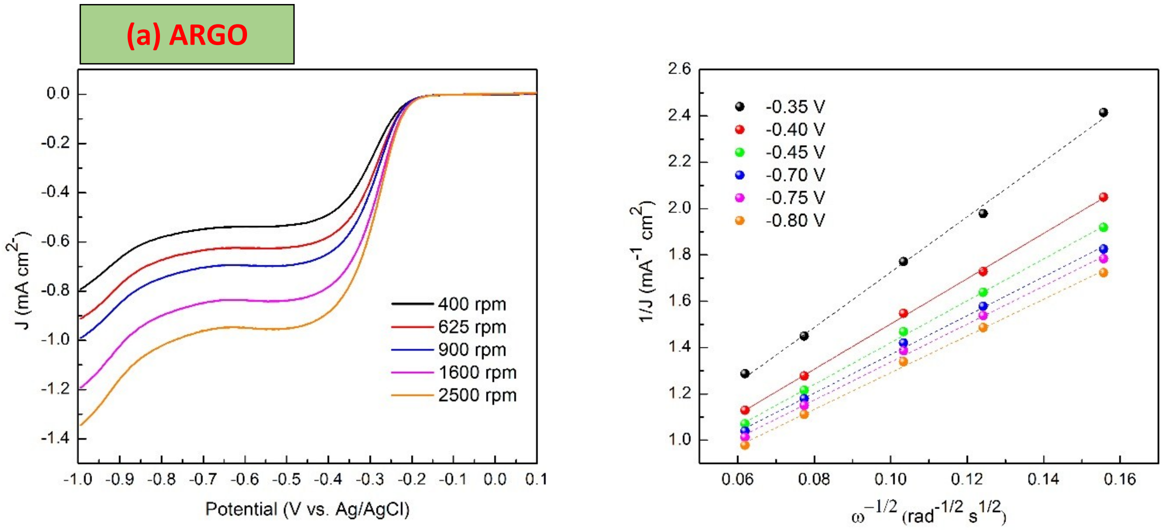
(a) ARGO
J (mA cm2-)
0.0
-0.2
-0.4
-0.6
-0.8
-1.0
-1.2
-1.4
400 rpm
625 rpm
900 rpm
1600 rpm
2500 rpm
-1.0 -0.9 -0.8 -0.7 -0.6 -0.5 -0.4 -0.3 -0.2 -0.1 0.0 0.1
Potential (V vs. Ag/AgCl)
1/J (mA-1 cm2)
2.6
2.4
2.2
2.0
1.8
1.6
1.4
1.2
1.0
-0.35 V
-0.40 V
-0.45 V
-0.70 V
-0.75 V
-0.80 V
0.06 0.08 0.10 0.12 0.14 0.16
ω-1/2 (rad-1/2 s1/2)

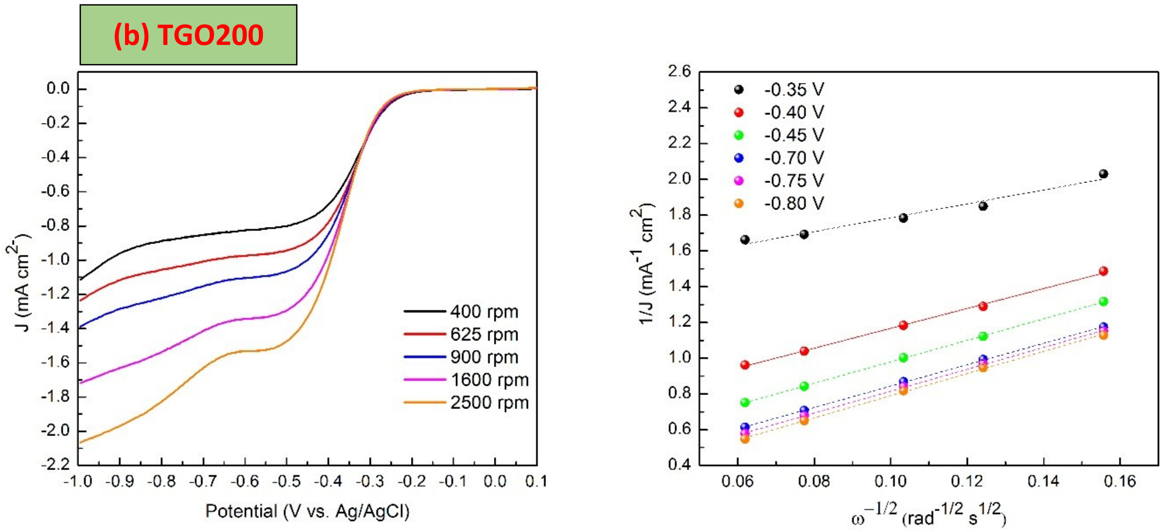
(b) TGO200
J (mA cm2-)
0.0
-0.2
-0.4
-0.6
-0.8
-1.0
-1.2
-1.4
-1.6
-1.8
-2.0
-2.2
400 rpm
625 rpm
900 rpm
1600 rpm
2500 rpm
-1.0 -0.9 -0.8 -0.7 -0.6 -0.5 -0.4 -0.3 -0.2 -0.1 0.0 0.1
Potential (V vs. Ag/AgCl)
1/J (mA-1 cm2)
2.6
2.4
2.2
2.0
1.8
1.6
1.4
1.2
1.0
0.8
0.6
0.4
-0.35 V
-0.40 V
-0.45 V
-0.70 V
-0.75 V
-0.80 V
0.06 0.08 0.10 0.12 0.14 0.16
ω-1/2 (rad-1/2 s1/2)

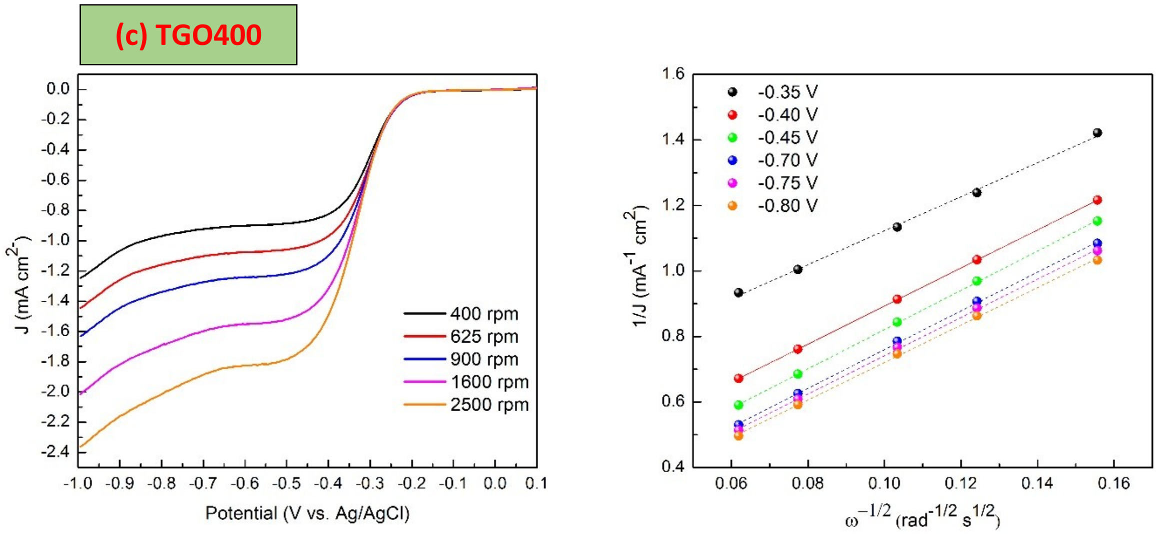
(c) TGO400
J (mA cm2-)
0.0
-0.2
-0.4
-0.6
-0.8
-1.0
-1.2
-1.4
-1.6
-1.8
-2.0
-2.2
-2.4
400 rpm
625 rpm
900 rpm
1600 rpm
2500 rpm
-1.0 -0.9 -0.8 -0.7 -0.6 -0.5 -0.4 -0.3 -0.2 -0.1 0.0 0.1
Potential (V vs. Ag/AgCl)
1/J (mA-1 cm2)
1.6
1.4
1.2
1.0
0.8
0.6
0.4
-0.35 V
-0.40 V
-0.45 V
-0.70 V
-0.75 V
-0.80 V
0.06 0.08 0.10 0.12 0.14 0.16
ω-1/2 (rad-1/2 s1/2)

(d) TGO600

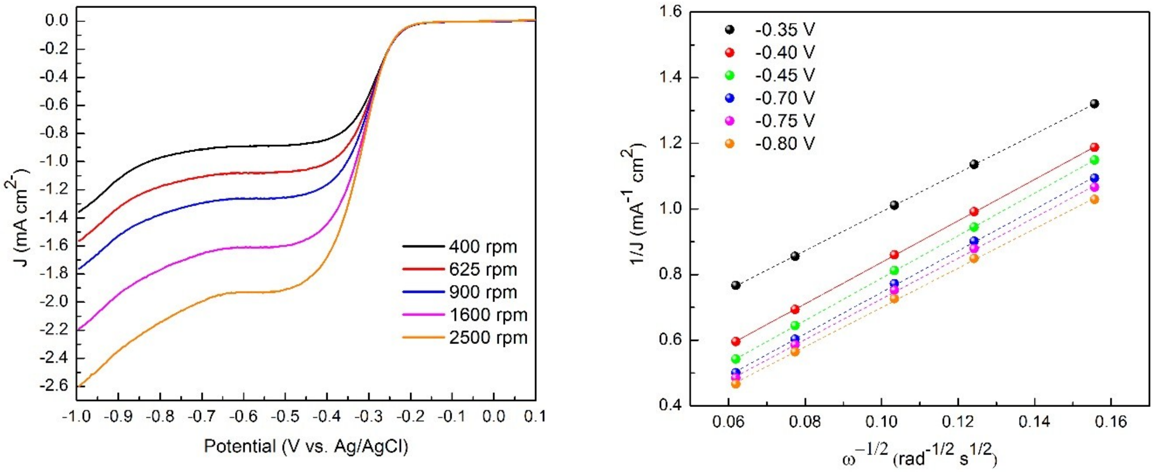

(e) TGO900

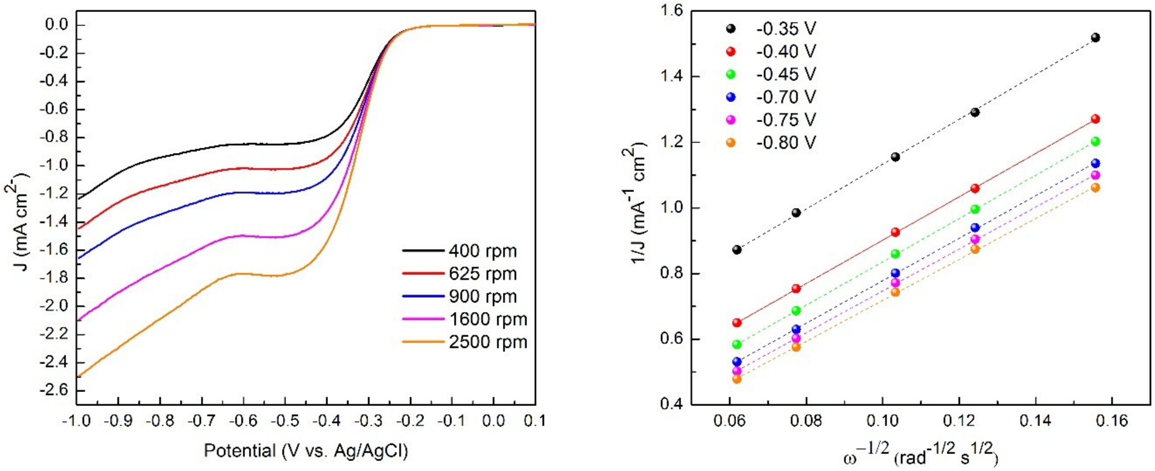

(f) CGO

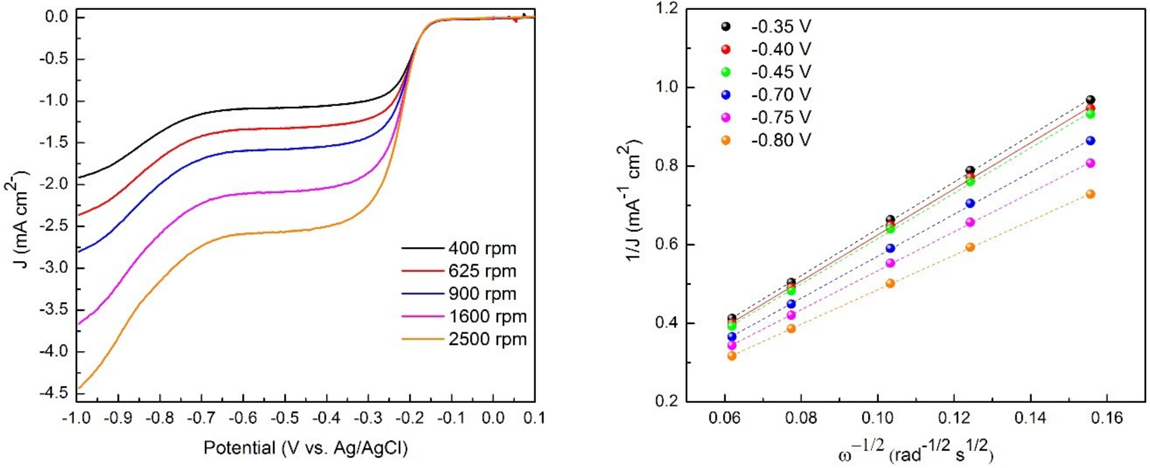

Figure S11. Polarization curves and K-L plots of (a) ARGO, (b) TGO200, (c) TGO400, (d) TGO600, (e) TGO900, and (f) CGO in O_2-saturated 1 M KOH electrolyte. Polarization curves were recorded at different rotation speeds of 400, 625, 900, 1600, and 2500 rpm. K-L plots were compiled at electrode potentials of -0.35, -0.40, -0.45, -0.70, -0.75 and -0.8 V, the slopes of the K-L plots were used to calculate the kinetic current density (J_k).

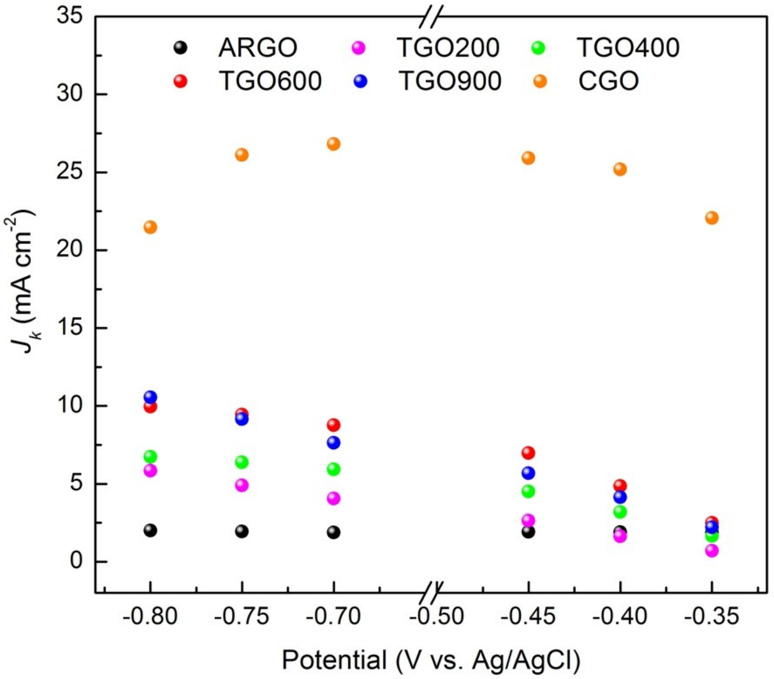

Figure S12. Kinetic limiting current density (J_k) of ARGO, TGOs, and CGO calculated from the corresponding K-L plots at different potentials (Figure S11). J_k reflects the intrinsic electrocatalytic ability of GO/rGO materials taking no account of the mass transport effect with regard to the oxygen absorption.

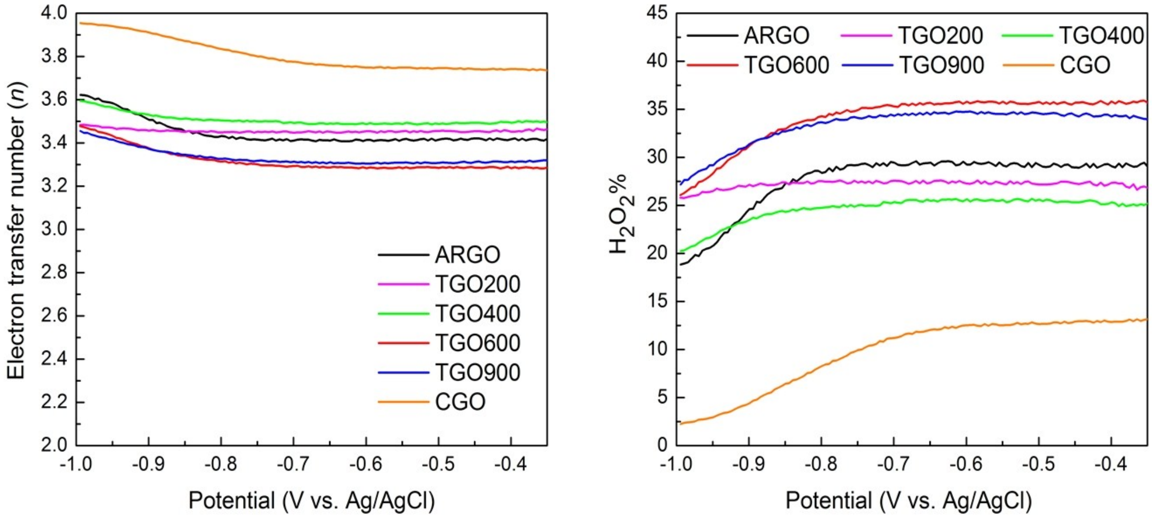

Figure S13. Electron transfer number (*n*) and H_2O_2 yield (% H_2O_2) of ARGO, TGOs, and CGO at various potentials from -0.35 to -0.1 V, which were determined based on the disk and ring currents measured from RRDE experiments.

REFERENCES

1. S. Liu, T. H. Zeng, M. Hofmann, E. Burcombe, J. Wei, R. Jiang, J. Kong and Y. Chen, *ACS Nano*, 2011, **5**, 6971-6980.
2. F. Perreault, A. F. de Faria, S. Nejati and M. Elimelech, *ACS nano*, 2015, **9**, 7226-7236.
3. O. Akhavan and E. Ghaderi, *ACS nano*, 2010, **4**, 5731-5736.
4. E. L. K. Chng and M. Pumera, *Chem. - Eur. J.*, 2013, **19**, 8227-8235.
5. Y. Chang, S.-T. Yang, J.-H. Liu, E. Dong, Y. Wang, A. Cao, Y. Liu and H. Wang, *Toxicol. Lett.*, 2011, **200**, 201-210.
6. C. K. Chua, Z. Sofer and M. Pumera, *Chem. - Eur. J.*, 2012, **18**, 13453-13459.
7. Y. L. F. Musico, C. M. Santos, M. L. P. Dalida and D. F. Rodrigues, *ACS Sustainable Chem. Eng.*, 2014, **2**, 1559-1565.
8. F.-C. Tai, S.-C. Lee, J. Chen, C. Wei and S.-H. Chang, *J. Raman Spectrosc.*, 2009, **40**, 1055-1059.
9. A. J. Glover, M. Cai, K. R. Overdeep, D. E. Kranbuehl and H. C. Schniepp, *Macromolecules*, 2011, **44**, 9821-9829.
10. M. Lotya, Y. Hernandez, P. J. King, R. J. Smith, V. Nicolosi, L. S. Karlsson, F. M. Blighe, S. De, Z. Wang and I. McGovern, *J. Am. Chem. Soc.*, 2009, **131**, 3611-3620.
11. K. Krishnamoorthy, M. Veerapandian, K. Yun and S. J. Kim, *Carbon*, 2013, **53**, 38-49.
12. G. A. Ferrero, K. Preuss, A. Marinovic, A. B. Jorge, N. Mansor, D. J. L. Brett, A. B. Fuertes, M. Sevilla and M.-M. Titirici, *ACS Nano*, 2016, **10**, 5922-5932.
13. Y. Liang, Y. Li, H. Wang, J. Zhou, J. Wang, T. Regier and H. Dai, *Nat. Mater.*, 2011, **10**, 780-786.
14. R. Zhou, Y. Zheng, M. Jaroniec and S.-Z. Qiao, *ACS Catal.*, 2016, **6**, 4720-4728.
15. Z. Chen, D. Higgins and Z. Chen, *Carbon*, 2010, **48**, 3057-3065.
16. I. Kruusenberg, N. Alexeyeva and K. Tammeveski, *Carbon*, 2009, **47**, 651-658.
17. L. M. Pasquini, R. C. Sekol, A. D. Taylor, L. D. Pfefferle and J. B. Zimmerman, *Environ. Sci. Technol.*, 2013, **47**, 8775-8783.
18. J. Benson, Q. Xu, P. Wang, Y. Shen, L. Sun, T. Wang, M. Li and P. Papakonstantinou, *ACS Appl. Mater. Interfaces*, 2014, **6**, 19726-19736.
19. Z.-J. Jiang and Z. Jiang, *Sci. Rep.*, 2016, **6**, 27081.
20. C. X. Guo, Y. Lei and C. M. Li, *Electroanalysis*, 2011, **23**, 885-893.
21. C. Guo, F. Hu, C. M. Li and P. K. Shen, *Biosens. Bioelectron.*, 2008, **24**, 819-824.
22. M. Acik, G. Lee, C. Mattevi, A. Pirkle, R. M. Wallace, M. Chhowalla, K. Cho and Y. Chabal, *J. Phys. Chem. C*, 2011, **115**, 19761-19781.
23. M. Fernandez-Merino, L. Guardia, J. Paredes, S. Villar-Rodil, P. Solis-Fernandez, A. Martinez-Alonso and J. Tascon, *J. Phys. Chem. C*, 2010, **114**, 6426-6432.
24. A. Mathkar, D. Tozier, P. Cox, P. Ong, C. Galande, K. Balakrishnan, A. Leela Mohana Reddy and P. M. Ajayan, *J. Phys. Chem. Lett.*, 2012, **3**, 986-991.
25. J. Li, G. Xiao, C. Chen, R. Li and D. Yan, *J. Mater. Chem. A*, 2013, **1**, 1481-1487.
26. W.-C. Hou, I. Chowdhury, D. G. Goodwin Jr, W. M. Henderson, D. H. Fairbrother, D. Bouchard and R. G. Zepp, *Environ. Sci. Technol.*, 2015, **49**, 3435-3443.
27. Y. Jiang, R. Raliya, J. D. Fortner and P. Biswas, *Environ. Sci. Technol.*, 2016, **50**, 6964-6973.